Journal of Materials Chemistry A

Accepted Manuscript

ROYAL SOCIETY OF CHEMISTRY

www.rsc.org/materialsA

Optimized Thermoelectric Properties in Pseudocubic Diamond-like $CuGaTe_2$ Compounds

Yuting Qin,[abc] Pengfei Qiu,[ab] Ruiheng Liu,[b] Yulong Li,[abc] Feng Hao,[abc] Tiansong Zhang,[ab] Dudi Ren, [ab]Xun Shi,[ab]* and Lidong Chen [abd]*

[a]CAS Key Laboratory of Materials for Energy Conversion,
Shanghai Institute of Ceramics, Chinese Academy of Science, Shanghai 200050, China

[b]State Key Laboratory of High Performance Ceramics and Superfine Microstructure,
Shanghai Institute of Ceramics, Chinese Academy of Science, Shanghai 200050, China

[c]University of Chinese Academy of Sciences, Beijing 100049, China

[d]Shanghai Institute of Materials Genome, Shanghai, China

* Email: xshi@mail.sic.ac.cn; cld@mail.sic.ac.cn

Abstract

The pseudocubic structure approach has been proposed recently to screen and design good thermoelectric materials via realizing overlapped band edges for excellent electrical transport properties. Diamond-like compound is a typical example agreeing the concept of pseudocubic structure by tuning its lattice distortion parameter to unity. However, besides band structure, the optimized carrier concentration and reduced lattice thermal conductivity are also required for high thermoelectric figure of merit (zT). In this work, taking $CuGaTe_2$ as an example, we have successfully demonstrated that Cu-deficiency can effectively tune carrier concentrations and In-alloying at Ga sites can effectively lower lattice thermal conductivity. By combining these two strategies, the electrical and thermal transports can be separately optimized in $CuGaTe_2$-based pseudocubic diamond-like compounds, leading to much enhanced zTs, about 24% improvement for $Cu_{0.99}In_{0.6}Ga_{0.4}Te_2$ at 800 K. Furthermore, the average zTs from 300 K to 800 K are improved by 87% as compared with $CuGaTe_2$ matrix. This study provides a promising way to optimize the

TE performance in the pseudocubic diamond-like compounds by simultaneously tuning electrical and thermal transports.

1. Introduction

Due to the increasing concern on global energy crisis, thermoelectric (TE) technology has attracted widespread attention as an alternative energy resource to reduce fossil-fuel consumption. The overall performance of a TE material is determined by its figure of merit (zT), defined as $zT = S^2\sigma T/\kappa$, where S is the Seebeck coefficient, σ is the electrical conductivity, κ is the thermal conductivity, and T is the absolute temperature. [1-8]

Ternary chalcopyrite compounds with the space group of I-42d represent a large family of materials. These compounds are derived from II-VI cubic zinc-blende but they have two kinds of cations orderly cross-substituted at Zn-site. Ternary chalcopyrite compounds display much lower thermal conductivity as compared with binary zinc blende because of the extra mass and strain fluctuations of the cations which can strongly scatter lattice phonons. In addition, the dominant covalent bonds in these chalcopyrite compounds ensure the character of semiconducting carrier conducting with moderate carrier mobility. All these indicate that chalcopyrite compounds may have promising TE performances. So far, the high zTs have been reported only in some chalcopyrite compounds such as $Cu_2ZnSn_{0.90}In_{0.10}Se_4$ (zT = 0.95 at 850 K),[1] $Cu_{2.10}Cd_{0.90}SnSe_4$ (zT = 0.65 at 700 K),[2] $Cu_{12-x}M_xSb_4S_{13}$ (M = Zn, Fe) (zT > 0.8 above 700 K),[3] $Cu_2Sn_{0.9}In_{0.1}Se_3$ (zT = 1.14 at 850 K),[4] $Ag_{0.95}GaTe_2$(zT = 0.77 at 850 K),[5] $CuInTe_2$ (zT = 1.18 at 850 K),[6] and $CuGaTe_2$ (zT = 1.4 at 950 K).[7]

However, many other chalcopyrite compounds still possess low TE figure of merit mainly due to the deteriorated electrical transport by the non-cubic crystal structure.

Recently, Zhang *et al*. have proposed pseudocubic structure approach to screen TE chalcopyrite compounds.[8] A simple unity-rule, defined by the structure distortion parameter $\eta=c/2a$ where c and a are the lattice parameters along the z-axes and x-axes, respectively, has been used to evaluate TE performance. When η is around 1, the band edges at the top of valence band are nearly overlapped (energy-splitting Δ_{CF} is 0), leading to a cubic-like degenerate band-edge electronic state for high power factor ($PF = S^2\sigma$) and zTs. $CuGaTe_2$ and $CuInTe_2$, as two typical examples, possess excellent TE properties with the zT around 1.2-1.4 because their η values are around unity.[6, 8] This makes them among the top bulk thermoelectric materials. A few efforts have been performed to optimize the TE properties of $CuGaTe_2$ and $CuInTe_2$ recently. The TE properties of $CuGaTe_2/xCu_2Se$ composites in a moderate temperature range have been investigated.[9] The maximum zT of the composites is 74% larger than that of the $CuGaTe_2$ matrix, which is attributed to the decrease of thermal conductivity and the improvement of electrical properties. Thermoelectric performance has been enhanced by Ag doping in $CuGaTe_2$ compounds due to the improved electrical conductivity and the reduced lattice thermal conductivity.[10] $Cu_{1-x}GaSb_xTe_2$ compounds have also been studied, but it turns out that Sb mostly occupies Te sites rather than Cu sites.[11] Also, optimized TE performance has been found in $CuIn_{1-x}Cd_xTe_2$ compounds due to the increase of hole concentration.[12] $CuInTe_2$/graphene composites have been studied and a zT of 0.4 at 700 K is achieved

with a mass ratio of 80:1.[13] Particularly, element alloying, the traditional method used for material' optimization, has been demonstrated theoretically as a very effective approach to realize pseudocubic structure in chalcopyrite compounds to optimize TE properties. This has been well displayed in Cu(Ga, In)Te_2 and (Ag, Cu)$InTe_2$ solid solutions in which the high *PF*s and *zT*s are reported.[8, 14] Furthermore, significant κ reduction is also achieved in these solid solutions due to the additional phonon point defect scatterings.[15]

As we know, alloying usually has a weak effect on carrier concentrations if the atomic ratios are well maintained while element doping with non-equivalent charge state can strongly change carrier concentrations. This can be supported by comparing the electrical properties of those doped and alloyed materials in Ref. 1-4, 10-12 and 14. Particularly, the carrier concentrations of $CuInTe_2$ and $CuGaTe_2$ are only around 10^{18} cm^{-3}, far less than the state of the art TE materials such as Cu_2Se (10^{20} cm^{-3}),[16] PbTe (10^{19} cm^{-3}),[17] filled-$CoSb_3$ (10^{20} cm^{-3}),[18] and Bi_2Te_3 (10^{19} cm^{-3}).[19] Element doping may change the crystal structure and thus deviate η value from unity. Consequently, the electrical transports can be greatly deteriorated. Except element doping, lattice defect is another effective approach to tune carrier concentrations.[20-24] In fact, the presence of Cu deficiency is a common inherent feature in Cu-based semiconductors. The strategy via artificially generating Cu deficiency to tune carrier concentrations has been successfully demonstrated in $Cu_{2-x}Se$ and $Cu_{2-x}S$.[14, 25, 26] Inspired by these recent works, we believe it is possible to tune charge carriers in chalcopyrite compounds by using Cu-deficiency.

In this work, we firstly show how Cu-deficiency changes electrical and thermal properties. Then the TE properties of Cu(Ga, In)Te_2 are reported. Finally, we combine these two strategies together by creating Cu-deficiency and alloying In at Ga site to optimize TE performance in the pseudocubic $CuGaTe_2$ compound. Significant optimized electrical properties, lowered thermal conductivity, and enhanced zTs in the diamond-like pseudocubic compounds through the entire temperature range are obtained.

2. Experiment Section

A series of $CuGaTe_2$-based materials with different chemical compositions have been prepared successively, including $Cu_{1-x}GaTe_2$ (x = 0, 0.01, 0.015, and 0.02), $CuGa_{1-y}In_yTe_2$ (y = 0, 0.2, 0.4, 0.6, 0.8, and 1), and $Cu_{1-x}(Ga_{1-y}In_y)Te_2$ (x = 0.01, 0.02, y = 0.2, 0.4, 0.6, and 0.8). High purity raw elements, Cu (shots, 99.999%, Alfa Aesar), Ga (shots, 99.9999%, Alfa Aesar), (shots, 99.999%, Alfa Aesar), and Te (shots, 99.999%, Alfa Aesar) were weighed out in stoichiometric proportions, sealed in quartz tubes under vacuum, and then melted at 1373 K for 12 h. Then, the tubes were quenched into cold water and annealed at 923 K for 5 days. To form densified pellets, the obtained ingots were ground into fine powders in an agate mortar and then sintered by Hot Pressing Sintering (MRF Inc., USA) for 30 minutes at 863 K. High-density samples (>99% of the theoretical density) were obtained.

X-ray diffraction (XRD) analyses (D8 ADVANCE, Bruker Co. Ltd) were employed to examine phase purity and chemical compositions of the samples. The microstructure analysis has been done by scanning electron microscopy (SEM, ZEISS

Supra 55). Electrical transport properties, including electrical conductivity and Seebeck coefficient, were measured by using ZEM-3 (ULVAC Co. Ltd.) apparatus under Helium atmosphere from 300 K to 800 K. The thermal diffusivities were measured in argon atmosphere by using laser flash method (NETZSCH LFA 427). The heat capacity for each sample is estimated by the *Neumann-Kopp* law.[27-28] The density of the samples was measured by using the *Archimedes* method. Thermal conductivity was calculated by using the specific heat, measured thermal diffusivity and sample density. Hall coefficients (R_H) from 2 K to 300 K were measured in a Quantum Design Physical properties measure system (PPMS) by sweeping the magnetic field up to 3 T in both positive and negative directions. The hole concentration (p) is calculated by $p = 1/ R_H e$, where e is the elementary charge. Hall carrier mobility (μ_H) was calculated according to the relation $\mu_H = R_H \sigma$.

3. Result and discussion

3.1. Cu-deficiency $Cu_{1-x}GaTe_2$ (x = 0, 0.01, 0.015, and 0.02)

3.1.1. Structural characterization

We firstly studied the Cu-deficiency samples with the designed compositions of $Cu_{1-x}GaTe_2$ (x= 0, 0.01, 0.015, and 0.02). Fig. 1 shows the XRD patterns for all the samples. Only the peaks in the chalcopyrite structure (PDF #47-1454) are observed, indicating that small amount of Cu-deficiency in $CuGaTe_2$ is allowed and the crystal structure is scarcely changed. Based on the lattice parameters (a, c) obtained by Rietveld structure refinement (WINCSD program package), the η value of each sample is calculated and listed in Table 1. All samples have almost the same η values,

suggesting that Cu-deficiency exerts little influence on the crystal structure. Since all η values are close to 1, the high-degree cubic-like degenerate band-edge electronic states should be preserved in these nonstoichiometric $Cu_{1-x}GaTe_2$ samples and thus good electrical transports are expected. The microstructure analysis has been done by SEM-EDS. Taking $Cu_{0.98}GaTe_2$ as an example (shown in Fig. 2), all elements are homogeneously distributed and no impurity phases are observed.

3.1.2. TE properties

The temperature dependences of electrical conductivity (σ), Seebeck coefficient (S), power factors (PFs), and thermal conductivity (κ) for all samples are shown in Fig. 3. In the whole temperature range, the σ for stoichiometric $CuGaTe_2$ increases monotonously with increasing temperature, showing typical intrinsic semiconducting behavior. The σ of $CuGaTe_2$ is in the order of 10^3 S/m around room temperature. When introducing Cu-deficiency into $CuGaTe_2$, the σ is greatly improved as shown in Fig. 3a and is in the order of 10^4 S/m in the whole measured temperature range. The maximum σ, around 7×10^4 S/m at 300 K, has been obtained in $Cu_{0.98}GaTe_2$, which is around 30 times higher than that in the $CuGaTe_2$ matrix at the same temperature. In addition, the difference of σ between Cu-deficiency samples and $CuGaTe_2$ matrix is much smaller at high temperature due to the increase of σ in $CuGaTe_2$ matrix. Furthermore, the temperature dependency is also changed and it gradually shifts to heavily-doped semiconducting behavior when increasing the amount of Cu-deficiency, as shown in Fig. 3a. Correspondingly, room temperature S (Fig. 3b) decreases with the increase of Cu-deficiency with the values of 413 μV/K in $CuGaTe_2$ and 129 μV/K

in $Cu_{0.98}GaTe_2$. The *PF*s are shown in Fig. 3c. As a result of the greatly enhanced σ and lowered *S* values, the overall *PF*s are increased in the nonstoichiometric $Cu_{1-x}GaTe_2$ samples especially in the low and medium temperature range. For instance, the *PF* in $Cu_{0.98}GaTe_2$ is enhanced by 245% and 57% as compared with the $CuGaTe_2$ matrix at 300 K and 700 K, respectively. These high *PF*s are also consistent with the concept of pseudocubic structure for high electrical transports because the η values in all $Cu_{1-x}GaTe_2$ samples are nearly around unity (see Table 1). The total κ is shown in Fig. 3d. The presence of Cu-deficiency scarcely reduces κ. Inversely, κ in the high temperature is even higher than the $CuGaTe_2$ compound due to the increase of electrical thermal conductivity in the samples with large Cu-deficiency.

Since the charge state of Cu is +1 in $CuGaTe_2$, Cu-deficiency means that less electrons are provided by the cations, thereby leading to large hole concentrations. Fig. 4a shows the temperature dependences of hole concentration *p*. All samples show p-type carrier conducting, which is consistent with the positive *S* values shown in Fig. 3b. The $CuGaTe_2$ shows a hole concentration in the order of 10^{18} cm^{-3} at room temperature, consistent with the values reported in Ref. 7. All the Cu-deficiency samples show hole concentrations in the range of 10^{19} cm^{-3}, one order of magnitude higher than that of $CuGaTe_2$ (Fig. 4a). This thus provides a good explanation to the observed increase of σ and decrease of *S* shown in Fig. 3a and 3b. The temperature dependences of Hall mobility (μ_H) are shown in Fig. 4b. $CuGaTe_2$ shows a dominant ionic impurity scattering between 50 K and 100 K but transits to acoustic phonon scattering near room temperature, probably due to its low carrier concentration. In the

Cu-deficiency samples, the dominant neutral scattering is observed at low temperatures but it turns to change to acoustic scattering near room temperature, displaying a mixture of neutral scattering and acoustic scattering. The similar μ_H variation trend is also observed in Cd doped $CuInTe_2$ compounds.[12] This can be explained by the greatly increased carrier concentrations as shown in Fig. 4a. When the carrier concentration is low, the Coulomb interaction in $CuGaTe_2$ compound is not fully screened, thus ionic scattering is the dominated mechanism. However, in the high carrier concentration samples, the very small Debye screen length strongly screened the Coulomb interaction, thus the ionic impurity scattering is much weakened and sometimes neglected.

Fig. 4c presented the lattice thermal conductivity (κ_L) as a function of temperature for $Cu_{1-x}GaTe_2$ (x = 0, 0.01, 0.015, and 0.2) compounds. The κ_L was calculated by $\kappa_L=\kappa-L\sigma T$, where L is the Lorenz constant，which is calculated according to Equation (1)

$$L = \left(\frac{k_B}{e}\right)^2 \left\{\frac{(\lambda+3)F_{\lambda+2}(\psi)}{(\lambda+1)F_\lambda(\psi)} - \left[\frac{(\lambda+2)F_{\lambda+1}(\psi)}{(\lambda+1)F_\lambda(\psi)}\right]^2\right\} \quad , (1)$$

where k_B is the Boltzmann constant, λ is the scattering factor, ψ (= E_F/k_BT) is the reduced Fermi energy, and the Fermi integrals are given by $F_n(\psi) = \int_0^\infty \frac{x^n dx}{1+exp(x-\psi)}$, where x is the reduced carrier energy.

Because of the small σ in $Cu_{1-x}GaTe_2$, the difference between κ and κ_L is very small. Because of the extra phonon scattering derived from lattice defects by Cu-deficiency, κ_L is decreased with the increase of Cu-deficiency. However, the κ_L reduction is very weak. For example, the κ_L is only reduced to 6.62 W/m-K in $Cu_{0.98}GaTe_2$ from 8.14

W/m-K in $CuGaTe_2$ at 300 K.

Although the reduction of κ_L is very small, the overall zTs of Cu-deficiency samples relatively increases through the whole temperature range. The maximum zT is increased from 0.66 in $CuGaTe_2$ to 0.73 in $Cu_{0.985}GaTe_2$ at 800 K. Furthermore, the average zT among a large temperature range is increased greatly, as shown in Fig. 4d.

3.2. $CuGa_{1-y}In_yTe_2$ (y = 0, 0.2, 0.4, 0.6, 0.8, and 1) solid solutions

Cu-deficiency can greatly affect carrier concentrations as well as electrical transports in $CuGaTe_2$. However, the reduction of thermal conductivity is very small. Alloying is a very effective approach to reduce thermal conductivity. Meanwhile it can efficiently adjust η to be around unity, thus causing high-degree cubic-like degenerate band-edge electronic states leading to good electrical properties. In this section, we systematically studied the TE properties of $Cu(Ga_{1-y}In_y)Te_2$ solid solutions.

3.2.1. Structural characterization

Fig. 5 shows the powder XRD patterns for $CuGa_{1-y}In_yTe_2$ (y = 0, 0.2, 0.4, 0.6, 0.8, and 1) samples. It is consistent with the ICSD PDF card with the number of PDF #47-1454, showing that all the samples have chalcopyrite structure and there are no impurity phases. The peak positions shift gradually to the low angle direction with the increase of In content due to the large atomic radius of In as compared with Ga. This suggests we have gotten a complete solid solution between $CuInTe_2$ and $CuGaTe_2$. The lattice constants c and a are obtained by Rietveld structure refinement (WINCSD program package). Then the η values are calculated and listed in Table 1. The η values are close to 1, suggesting solid-solutions are within the concept of pseudocubic

structure approach. The SEM-EDS results of $CuGa_{0.6}In_{0.4}Te_2$ in Fig. 6 display very uniform element distributions, no impurity phase are observed, which is completely consistent with the XRD results.

3.2.2. TE properties

The temperature dependence of electrical conductivity (σ), Seebeck coefficient (S), power factors (PFs), and thermal conductivity (κ) for $CuGa_{1-y}In_yTe_2$ (y = 0, 0.2, 0.4, 0.6, 0.8, and 1) compounds are shown in Fig. 7. All samples display similar temperature-dependence, a typical semiconducting behavior. The σ increases quickly with increasing temperature. In addition, the electrical conductivity σ increases with the increase of Ga content. It's probably because the electronegativity difference between Cu (1.9) and Ga (1.81) is smaller than that between Cu (1.9) and In (1.78), leading to the increased covalent character for high carrier mobility. In addition, the decreased effective mass in $CuGa_{1-y}In_yTe_2$ may also lead to large carrier mobility when increasing Ga content. Correspondingly, the change of S displays opposite direction. The S decreases when increasing Ga content. Because In and Ga have almost the same valence state, the differences among σ and S in $CuGa_{1-y}In_yTe_2$ solid solutions are not large with a maximum deviation of about 30% for σ at 800 K and 20% for S at 400 K. Consequently, the PFs for $CuGa_{1-y}In_yTe_2$ (y = 0, 0.2, 0.4, 0.6, 0.8, and 1) compounds are roughly equivalent with the maximum value of 12.2 μW/cm-K^2 at 800 K. The temperature dependence of thermal conductivity κ is shown in Fig. 7d. The lowest κ is reduced to 3.76 W/m-K at 300 K and 1.04 W/m-K at 800 K, 54% and 35% reduction respectively as compared with $CuGaTe_2$. Obviously, the reduction is

very great as compared with the data for Cu-deficiency samples shown in section 2.1.

The temperature dependence of hole concentration and Hall mobility from 2 K to 300 K are displayed in Fig. 8a and Fig. 8b, respectively. All the hole concentrations are in the magnitude of 10^{18} cm^{-3} at room temperature. As we expected, because In and Ga have similar charge states, the difference in hole concentration is very small. For example, the largest deviation in hole concentration at room temperature is only 0.04×10^{18} cm^{-3}. Similar to hole concentration, the Hall mobilities among all samples are also very alike. All $CuGa_{1-y}In_yTe_2$ (y = 0, 0.2, 0.4, 0.6, 0.8, and 1) compounds display $\mu_H \propto T^{-3/2}$ dependence near room temperature, indicating that the acoustic phonon scattering is the dominated charge carrier scattering mechanism. Below 100 K, it matches well with $\mu_H \propto T^{3/2}$ dependence, which is ascribed to the dominated ionic impurity scattering.[12, 29]

The temperature dependence of lattice thermal conductivity κ_L for $CuGa_{1-y}In_yTe_2$ (y = 0, 0.2, 0.4, 0.6, 0.8, and 1) compounds is demonstrated in Fig. 8c. Similar to the Cu-deficiency samples as shown in section 3.1, the electrical thermal conductivity is so small that the lattice thermal conductivity dominates the total thermal conductivity. Thus, the lattice thermal conductivity κ_L is very close to the total thermal conductivity κ. The largest deviation for κ_L from the respective total thermal conductivity κ among all the $CuGa_{1-y}In_yTe_2$ (y = 0, 0.2, 0.4, 0.6, 0.8, 1) samples is only about 0.2%. However, the κ_L in the solid-solution samples is greatly reduced by comparing to $CuGaTe_2$ and $CuInTe_2$ compounds due to the strong phonon defect scatterings when alloying In at Ga sites. Overall, the thermal conductivity in $CuGa_{1-y}In_yTe_2$

solid-solutions is greatly reduced while the electrical properties are well maintained. As a result, the TE performance is evidently enhanced. The maximum zT in the solid-solution samples is 0.84 at 800 K, which is about 27% larger than the $CuGaTe_2$ compound.

3.3. Cu-deficient $Cu_{1-x}(Ga_{1-y}In_y)Te_2$ (x = 0.01 and 0.02, y = 0.2, 0.4, 0.6, and 0.8) solid solutions

Introducing Cu-deficiency into $CuGaTe_2$ greatly increases carrier concentrations as well as changes electrical properties, but thermal conductivity is reduced very weakly. Alloying In at Ga sites significantly lowers thermal conductivity, but the electrical properties are nearly unaffected.

In this section, we combine the strategies of generating Cu-deficiency and alloying In at Ga sites to tune electrical and thermal properties simultaneously.

3.3.1. Structural characterization

The powder XRD patterns are displayed in Fig. 9. No diffraction peaks belonging to the secondary phase are detected in $Cu_{1-x}(Ga_{1-y}In_y)Te_2$ (x = 0.01 and 0.02, y = 0.2, 0.4, 0.6 and 0.8) samples, agreeing well with the ICSD PDF card (PDF #47-1454). The lattice constants a and c are refined with WINCSD package program and the distortion parameter η is calculated. The η results for all $Cu_{1-x}(Ga_{1-y}In_y)Te_2$ (x = 0.01 and 0.02, y = 0.2, 0.4, 0.6, and 0.8) samples are list in Table 1. All the samples own approximately unity η, indicating considerable electrical performance. Fig. 10 shows the SEM images of $Cu_{0.98}Ga_{0.6}In_{0.4}Te_2$ compound as one example. The EDS results undoubtedly verifies that the samples are pure phase.

3.3.2. TE properties

The electrical conductivity (σ), Seebeck coefficient (S), power factors (PFs), and thermal conductivity (κ) as a function of temperature are shown in Fig. 11. As we expected, the electrical properties are mainly determined by the content of Cu-deficiency. Since three different levels of Cu-deficiency are used in this section, the electrical transports display three different trends, especially for electrical conductivity. Similar to section 3.1, the presence of Cu-deficiency greatly improves electrical conductivity. The Seebeck coefficient S decreases accordingly. The samples with Cu-deficiency display with a transform from semiconductor conducting to metallic conducting behavior. Thus the PFs are boosted through all the temperature range, especially at intermediate temperature. The maximum PF is 13.53 μW/cm-K^2 for $Cu_{0.98}(Ga_{0.6}In_{0.4})Te_2$, increased by almost 37% at 650 K as compared with the value of 9.89 μW/cm-K^2 in $CuGaTe_2$. The temperature dependence of thermal conductivity κ is shown in Fig. 11c. As we have shown in section 3.2, a small amount of In alloying can greatly lower κ. This is also observed in Cu-deficiency solid solutions. When combining alloying with Cu-deficiency, the thermal conductivity is reduced obviously due to the phonon scatterings, despite the small reduction of thermal conductivity causing by Cu-deficiency separately.

Fig. 12a shows the hole concentrations of $Cu_{1-x}(Ga_{1-y}In_y)Te_2$ (x = 0.01 and 0.02, y = 0.2, 0.4, 0.6, and 0.8) compounds. The hole concentrations increase at least one order of magnitude as compared with $CuGaTe_2$ mainly due to the effect of Cu-deficiency (see Fig. 12a). The Hall mobilities μ_H are shown in Fig. 12b. $Cu_{1-x}(Ga_{1-y}In_y)Te_2$ compounds show weakly temperature dependence of μ_H below 100 K. It becomes

relatively close to $\mu_H \propto T^{-3/2}$ dependence above 100 K. This indicates a mixture of charge carrier scattering mechanisms including acoustic phonon and neutral impurity scatterings.

Fig. 12c shows that the hole concentration changes little in the compounds with the same content of Cu-deficiency despite a great composition change of In that varies from 0 to 100%. Oppositely, the hole concentrations in the samples with same In content show an abrupt change by one order of magnitude when varying Cu-deficiency by only 2%. This strongly suggests that the hole concentrations are mainly affected by Cu-deficiency instead of In alloying, which are well consistent with section 3.3.1 and 3.3.2. Similar phenomenon has also been observed in carrier mobility (see Fig. 12d). The samples with the same Cu-deficiency own comparable carrier mobility despite the In content varying from 0 to 100% while the samples with different Cu-deficiencies have an apparently decrease when x changes only from 0 to 2%.

The lattice thermal conductivity κ_L for $Cu_{1-x}Ga_{1-y}In_yTe_2$ (x = 0.01 and 0.02; y = 0.2, 0.4, 0.6 and 0.8) samples are displayed in Fig. 12e. Obviously, κ_L is reduced greatly and quite similar in all the solid solutions due to the effect of both Cu-deficiency and In/Ga alloying. The zTs for $Cu_{1-x}(Ga_{1-y}In_y)Te_2$ (x = 0.01 and 0.02, y = 0.2, 0.4, 0.6, 0.8) samples are increased obviously through the whole temperature range. Because of the simultaneously enhanced σ and reduced κ, the maximum zTs, around 0.82 at 800 K, has been obtained in $Cu_{0.99}In_{0.6}Ga_{0.4}Te_2$, which is about 24% enhancement as compared with the matrix.

3.4. Discussion of transport properties

3.4.1. Electrical transports

Combining the single parabolic band model with the relaxation time approximation, the Seebeck coefficient S and carrier concentration p are described as[12, 30]:

$$S = \frac{k_B}{e}\left(\frac{(2+\lambda)F_{1+\lambda}(\psi)}{(1+\lambda)F_{\lambda}(\psi)} - \psi\right) \qquad (2)$$

and

$$p = 4\pi\left(\frac{2m^* k_B T}{h^2}\right)^{\frac{3}{2}} F_{\frac{1}{2}}(\psi) \qquad , (3)$$

where h is the Planck constant and m* is the effective mass. Assuming acoustic phonon scattering is the predominant carrier scattering mechanism near room temperature (λ=0), the effective mass m^* is calculated based on the measured S and p. Table 1 lists the m^* values for all samples. The m^* is 1.1-1.27 m_e for nonstoichiometric $Cu_{1-x}GaTe$ (x = 0.01, 0.015, and 0.02), 0.84-1.06 m_e for $CuGa_{1-y}In_yTe_2$ (y = 0.2, 0.4, 0.6, and 0.8), and 0.86-1.12 m_e for $Cu_{1-x}(Ga_{1-y}In_y)Te_2$ (x = 0.01 and 0.02, y = 0.2, 0.4, 0.6, and 0.8) compounds. This is a very small difference in m^* among the stoichiometric and nonstoichiometric samples. In Fig. 13b, we use the value of 1.1 m_e for m^* to calculate Seebeck coefficient and it shows a good agreement with the experiment data.

The trend line of experimental data shown in Fig. 14 indicates the optimum carrier concentration, corresponding to the best electrical transports in $CuGaTe_2$, is around $(1.0\text{-}3.0)\times10^{19}$ cm^{-3}. Interestingly, this range is quite similar with the optimum carrier concentration observed in $CuInTe_2$ system, being about $(1.5\text{-}3.7)\times10^{19}$ cm^{-3}. In fact, such consistency between these two systems has been also found in m^* values. For

example, under similar carrier concentrations (about 4.2-4.9×10^{19} cm^{-3}), the calculated m^* is 1.16 m_e for $CuInTe_2$ and 1.10 m_e for $CuGaTe_2$.[17] This suggests that $CuGaTe_2$ and $CuInTe_2$ should have similar band structures. Consequently, the $Cu_{1-x}(Ga_{1-y}In_y)Te_2$ solid solutions are expected to possess similar band structures too. The general trends in Fig. 14 strongly supports this augment.

3.4.2. Thermal transports

The lattice thermal resistivity (W = 1/κ) at 300 K for $Cu_{1-x}(Ga_{1-y}In_y)Te_2$ (x = 0, 0.01, and 0.02, y = 0, 0.2, 0.4, 0.6, and 0.8) compounds as a function of y is shown in Fig. 15. As shown in section 3.1, the presence of Cu-deficiency exerts little influence on the thermal transports, which is further confirmed by comparing the lattice thermal resistivity among all the samples shown in Fig. 15. Then we run the model calculation in the following part and the contribution of Cu-deficiency is ignored.

The solid line in Fig. 15 is calculated according to Callaway and Von Baeyer's theory, which is applied to solid-solution by Abeles later.[31-35] In the case of $CuGa_{1-y}In_yTe_2$ (y = 0, 0.2, 0.4, 0.6, 0.8, and 1) solid solutions, the thermal conductivity can be defined as:$\kappa_P = k_B/[4\pi v_m(ACT)^{\frac{1}{2}}]$. v_m is the simple average sound velocity of $CuGaTe_2$,which can be calculated by $v_m = \frac{2v_s}{3} + \frac{v_l}{3}$. Here v_s is the shear velocity of sound (2072 m/s), v_l is the longitudinal velocity of sound (3817 m/s).[7] CT is the relaxation time of phonon-phonon scattering, which is calculated by the experimental thermal conductivity of $CuGaTe_2$ at 300 K by using $\kappa_{pure} = \kappa_B^2\theta/(2\pi^2 v_s \hbar CT)$. The calculated CT is 9.65×10^{-16} s. A is the coefficient for the Rayleigh-type point-defect scattering rate:$t_{pd}^{-1} = A\omega^4$ (ω is the phonon frequency), which is given by A =

$\Omega_0\Gamma/(4\pi v_s^3)$, where Ω_0 is the unit cell volume. For single site impurity in $CuGa_{1-y}In_yTe_2$, Γ can be determined as: $\Gamma = y(1-y)(\Delta M/M_{av})^2$,where y is the concentration of Indium, ΔM is the mass difference between the impurity and the host, M_{av} is defined as the average mass of the compound:$M_{av} = \Sigma f_i M_i$,where f_i and Mi represents the fraction and the mass of impurity atom i respectively. Here, the effect of strain fluctuation is ignored due to the small difference in lattice constants between $CuInTe_2$ and $CuGaTe_2$ (about 3%, see in Table 1). Thus, $\Gamma_{Ga} = y(1\text{-}y)\left(\frac{45.097}{69.723+45.097y}\right)^2$.

For a compound such as $U_uV_vW_w$, the composite Γ can be defined as:

$$\Gamma(U_uV_VW_w) = \frac{u}{u+v+w}\left(\frac{M_U}{M_m}\right)^2\Gamma(U) + \frac{v}{u+v+w}\left(\frac{M_V}{M_m}\right)^2\Gamma(V) + \frac{w}{u+v+w}\left(\frac{M_w}{M_m}\right)^2\Gamma(W). \quad (4)$$

Here $M_m = (uM_U + vM_V + wM_W)/(u+v+w)$. In $CuGa_{1-y}In_yTe_2$ solid solution, U=(Cu), V=(In, Ga), W=(Te). Thus $\Gamma_{CuGaTe2} \approx \frac{1}{4}(69.723/97.117)^2\Gamma_{Ga}$ $A = 1.18 \times 10^{-37}\frac{y(1-y)}{(69.723+45.097y)^2}s^3$. The thermal resistivity W caused by solid solution formation is $W = \frac{4\pi v_m(ACT)^{\frac{1}{2}}}{k_B} = 25.98\frac{\sqrt{y(1-y)}}{69.723+45.097y}$. Fig. 15 displays the lattice thermal resisitivity across the solid solution from $CuGaTe_2$ to $CuInTe_2$. The dashed line is the ideal lattice thermal resistivity variation from the rule of mixtures of $CuGa_{1-y}In_yTe_2$ (y = 0, 0.2, 0.4, 0.6, 0.8, and 1) solid solutions. The solid line is the calculated lattice thermal resistivity caused by solid solutions using the above equations, which shows good consistency with our experimental data. This indicates that the κ_L reduction is mainly due to the mass fluctuations between In and Ga atoms.

3.4.3. TE performance vs structural distortion parameters η

As shown in Fig. 12f, the Cu-deficiency and In-alloying samples have greatly enhanced zTs as compared with the $CuGaTe_2$ matrix. The averaged zTs from 300 K to

800 K are displayed in Fig. 16a. Apparently, the averaged *zT*s are greatly improved from the matrix to Cu-deficiency samples, and finally to Cu-deficiency and In-alloying samples. For example, the average *zT*s between 300 K and 800 K for $CuGaTe_2$ is 0.22. It is increased to about 0.3 for $Cu_{1-x}GaTe_2$ (x = 0.01, 0.015, and 0.02) and $CuGa_{1-y}In_yTe_2$ (y = 0.2, 0.4, 0.6, and 0.8) compounds, and finally close to 0.4 for $Cu_{1-x}Ga_{1-y}In_yTe_2$ (x = 0.01 and 0.02; y = 0.2, 0.4, 0.6, and 0.8) samples. Fig. 16b shows the zT enhancement $\Delta(zT)/zT$ as compared with the $CuGaTe_2$ matrix. Obviously, the zT enhancement is much more significant in $Cu_{1-x}Ga_{1-y}In_yTe_2$ than that in $CuGa_{1-y}In_yTe_2$ and $Cu_{1-x}GaTe_2$, proving that simultaneously adopting both In alloying at Ga-site and creating deficiency at Cu-site is more effective to enhance *zT*s. Especially, such great zT enhancement occurs not only at the peak temperature but also throughout the whole temperature range, especially at low temperatures. This is quite meaningful for enhancing energy conversion efficiency in real applications.

Fig. 17a and 17b show the *PF*s at 300 K and 700 K as a function of distortion parameter η. All the samples with η around 1 possess good electrical transports and the peak can only be obtained around $\eta = 1$. This shows a good agreement with unity-η rule. Because the electrical transports dominate the TE performance in diamond-like compounds, the *zT*s show a similar trend to the *PF*s (See Fig. 17c). The literature *PF*s and *zT*s are from Ref. 1, 5-7, 36-39. Only the materials with $\eta = 1$ can realize high figure of merit. When η is shifted from 1, the *zT*s are dropped quickly. Therefore, the high *zT*s are observed in almost all of the materials. Fig. 17d shows η as a function of lattice parameter a. Both $CuInTe_2$ and $CuGaTe_2$ have η near 1. But it

is larger than 1 in $CuInTe_2$ and smaller than 1 in $CuGaTe_2$. As we expected, both calculations and experiment data show that the η in Cu(Ga, In)Te_2 solutions is almost between these two matrix and thus the η values in all the solutions are near 1. This indicates that the Cu(Ga, In)Te_2 solutions should also possess good electrical transports as well as *zT*s. Thus we can use this map to screen and design good TE materials. The TE transport data shown in this work well reflects the above augment. This means that once the carrier concentrations in Cu(Ga, In)Te_2 solutions are optimized, the high *zT*s will be expected and obtained.

4. Conclusion

We have successfully fabricated a series of $CuGaTe_2$–based pseudocubic diamond-like compounds via Cu-deficiency and In-alloying. We have systematically studied the crystal structures and thermoelectric properties. X-ray patterns and Rietveld structure refinement have been done to validate the chalcopyrite structures for all the samples. Firstly, $Cu_{1-x}GaTe_2$ (x = 0, 0.01, 0.015, 0.02) samples own almost unchanged η and greatly enhanced carrier concentrations and electrical conductivity but relatively small reduction in thermal conductivity. Secondly, we demonstrate that the η for $CuGa_{1-x}In_xTe_2$(x = 0, 0.2, 0.4, 0.6, 0.8, 1) solutions are extremely close to 1 and the thermal conductivity is reduced effectively while the changes in carrier concentrations and electrical transports are very small. Finally, we combine these two approaches to prepare $Cu_{1-x}Ga_{1-y}In_yTe_2$ (x = 0.01, 0.02; y = 0.2, 0.4, 0.6 and 0.8) compounds. Because of the increased hole concentrations by the Cu-deficiency and suppressed thermal conductivity by the In-alloying, significantly enhanced

thermoelectric performance has been achieved throughout the whole measured temperature range. The maximum average *zT* between 300 K and 800 K is increased by 87% as compared with $CuGaTe_2$ matrix. This work demonstrates that Cu-deficiency and In-alloying can separately optimize the electrical and thermal transports in $CuGaTe_2$–based compounds. It implies a promising way to optimize the TE performance in the pseudocubic diamond-like compounds.

Acknowledgements

This work is supported by National Basic Research Program of China (973-program) under Project No. 2013CB632501, National Natural Science Foundation of China (NSFC) under the No. 11234012 and 51302300, the Key Research Program of Chinese Academy of Sciences (Grant No. KGZD-EW-T06), and Shanghai Government (Grant No. 15JC1400301).

Reference

1 X. Y. Shi, F. Q. Huang, M. L. Liu and L. D. Chen. *Appl. Phys. Lett.*, 2009, **94**, 122103.

2 M. L. Liu, I. W. Chen, F. Q. Huang and L. D. Chen, *Adv. Mater.*, 2009, **21**, 3808.

3 X. Lu, D. T. Morelli, Y. Xia, F. Zhou, V. Ozolins, H. Chi, X. Y. Zhou and C. Uher, *Adv. Energy. Mater*., 2013, **3**, 342.

4 X. Y, Shi, L. L. Xi, J. Fan, W. Q. Zhang and L. D. Chen. *Chem. Mater*., 2010, **22**, 6029.

5 A. Yusufu, K. Kurosaki, A. Kosuga, T. Sugahara, Y. Ohishi, H. Muta and S. Yamanaka, *Appl. Phys. Lett.*, 2011, **99**, 061902.

6 R. H. Liu, L. L. Xi, H. L. Liu, X. Shi, W. Q. Zhang and L.D. Chen, *Chem. Commun*., 2012, **48**, 3818.

7 T. Plirdpring, K. Kurosaki, A. Kosuga, T. Day, S. Firdosy, V. Ravi, G. J. Snyder, A. Harnwunggmoung, T. Sugahara, Y. Ohishi, H. Muta and S. Yamanaka, *Adv. Mater.*, 2012, **24**, 3622.

8 J. W. Zhang, R. H. Liu, N. Cheng, Y. B. Zhang, J. H. Yang, C. Uher, X. Shi, L. D. Chen and W. Q. Zhang. *Adv. Mater.*, 2014, **26**, 3848.

9 J. Zhang, X. Y. Qin, D. Li, H. X. Xin, C. J. Song, L. L. Li, X. G. Zhu, Z. M. Wang, G. L. Guo and L. W, *J. Mater. Chem. A*. 2014, **2**, 2891.

10 J. Zhang, X. Y. Qin, D. Li, H. X. Xin, C. J. Song, L. L. Li, Z. M. Wang, G. L. Guo and L. Wang, *J. Alloy. Compd.*, 2014, **586**, 285.

11 J. L. Cui, Y. P. Li, Z. L. Du, Q. S. Meng and H. Zhou. *J. Mater. Chem. A.*, 2013, **1**, 677.

12 N. Cheng, R. H. Liu, S. Q. Bai, X. Shi and L. D. Chen, *J. Appl. Phys.*, 2014, **115**, 163705.

13 H. J. Chen, C. Y. Yang and F. Q. Huang, *CrystEngComm*., 2013, **15**, 6648.
14 Y. P. Li, Q. S. Meng, Y. Deng, H. Zhou and Y. L. Gao, *Appl. Phys. Lett.*, 2012, **100**, 231903.
15 H. Wang, A. D. LaLonde, Y. Z. Pei and G. J. Snyder, *Adv. Funct. Mater.*, 2013, **23**, 1586.
16 H. L. Liu, X. Shi, F. F. Xu, L. L. Zhang, W. Q. Zhang and L. D. Chen, Q. Li, C. Uher, T. Day, G. J. Snyder, *Nat. Mater.*, 2012, **11**, 422.
17 Y. Z. Pei, A. LaLonde, S. Iwanaga and G. J. Snyder, *Energy. Environ. Sci.*, 2011, **4(6)**, 2085.
18 X. Shi, H. Kong, C. P. Li, C. Uher and J. Yang, *Appl. Phys. Lett.*, 2008, **92**, 182101.
19 J. Suh, K. M. Yu, D. Y. Fu, X. Y. Liu, F. Yang, J. Fan, D. J. Smith, Y. H. Zhang, J. K. Furdyna, C. Dames, W. Walukiewicz and J. Q. Wu, *Adv. Mater.*, 2015, **27**, 3682.
20 L. P. Hu, T. J. Zhu, X. H. Liu, and X. B. Zhao, *Adv. Funct. Mater.*, 2014, **24**, 5211–5218.
21 G. Y. Jiang, J. He, T. J. Zhu, C. G. Fu, X. H. Liu, L. P. Hu and X. B. Zhao, *Adv. Funct. Mater.*, 2014, **24**, 3776–3781.
22 Y. T. Qiu, L. L. Xi, X. Shi, P. F. Qiu, W. Q. Zhang, L. D. Chen, J. R. Salvador, J. Y. Cho, J. H. Yang, Y. C. Chien, S. W. Chen, Y. L. Tang, G. J. Snyder, *Adv. Funct. Mater.*, 2013, **23**, 3194–3203.
23 Y. T. Qiu, J. J. Xing, X. Gao, L. L. Xi, X. Shi, H. Gu, L. D. Chen, *J. Mater. Chem. A.*, 2014, **2**, 10952–10959.
24 X. B. Wang, P. F. Qiu, T. S. Zhang, D. D. Ren, L. H. Wu, X. Shi, J. H. Yang and L.D. Chen, *J. Mater. Chem. A*, 2015, **3**, 13662.
25 Y. He, T. Day, T. S. Zhang, H. L. Liu, X. Shi and L. D. Chen, *Adv. Mater.*, 2014, **26**, 3975.
26 Y. He, T. S. Zhang, X. Shi, S. -H. Wei and L. D. Chen, *NPG Asia Mater.*, 2015, **7(8)**, e210.
27 H. Kopp, *Phil. Trans. R. Soc. Lond.*, 1865, **155**, 71.
28 J. Leitner, P. Vonka, D. Sedmidubsky, P. Svoboda, *Thermochimica Acta*, 2010, **497**, 7–13.
29 J. Y. Cho, X. Shi, J. R. Salvador, G. P. Meisner, J. Yang, H. Wang, A. A. Wereszczak, X. Zhou and C. Uher, *Phys. Rev. B*., 2011, **84**, 085207.
30 B. Kuhn, W. Kaefer, K. Fess, K. Friemelt, C. Turner, M. Wendl and E. Bucher, *Phys. Status. Solidi. A*., 1997, **162**, 661.
31 P. G. Klemens, *Phys. Rev.*, 1960, **119**, 507.
32 J. Callaway and H. C. von Baeyer, *Phys. Rev.*, 1960, **120**, 1149.
33 A. Abeles, *Phys. Rev.*, 1963, **131**, 1906.
34 G. P. Meisner, D. T. Morelli, S. Hu, J. Yang and C. Uher, *Phys. Rev.*, 1998, **80**, 16.
35 X. Shi, J. Yang, S. Q. Bai, J. H. Yang, H. Wang, M. F. Chi, J. R. Salvador, W. Q. Zhang, L. D. Chen and W. Wong-Ng. *Adv. Funct. Mater.*, 2010, **20**, 761.
36 M. Ibanez, R. Zamani, A. LaLonde, D. Cadavid, W. Li, A. Shavel, J. Arbiol, J. R. Morante, S. Gorsse, G. J. Snyder and A. Cabot, *J. Am. Chem. Soc.*, 2012, **134**,

4060.
37 P. Z. Ying, H. Zhou, Y. L. Gao, Y. Y. Li, Y. P. Li, X. L. Lian and J. L. Cui, *Key Eng. Mater.* 2012, **519**, 188.
38 A. Yusufu, K. Kurosaki, A. Kosuga, T. Sugahara, Y. Ohishi, H. Muta and S. Yamanaka, *Appl. Phys. Lett.* 2011, **99**, 061902.
39 Y. Li, Q. Meng, Y. Deng, H. Zhou, Y. Gao, Y. Li, J. Yang and J. Cui, *Appl. Phys. Lett.* 2012, **100**, 231903.

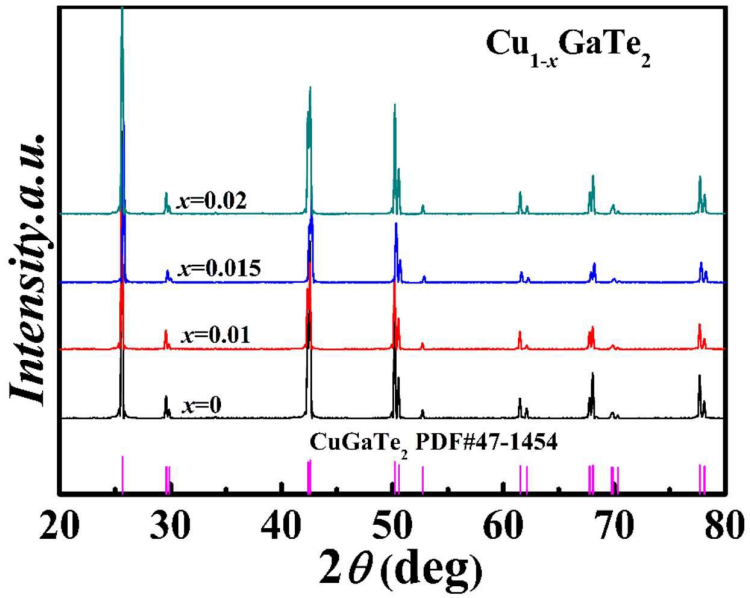

Fig. 1 Powder XRD patterns for $Cu_{1-x}GaTe_2$ (x = 0, 0.01, 0.015, and 0.2) compounds.

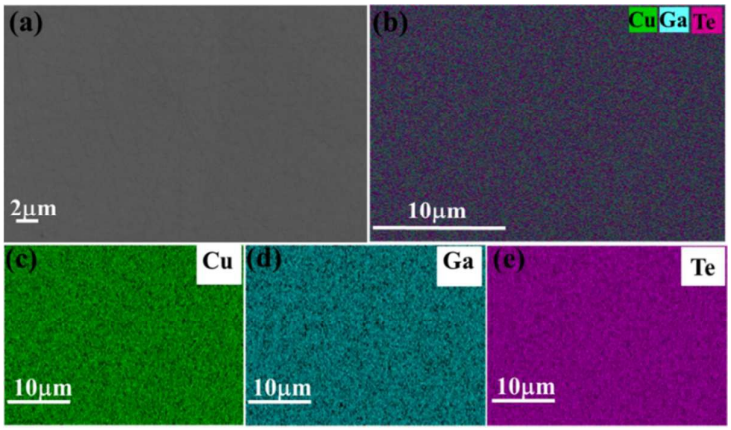

Fig. 2 Scanning electron microscopy (SEM) images of $Cu_{0.98}GaTe_2$ compound. (a) Backscattered electron imaging map, (b) all element, (c) Cu, (d) Ga, and (f) Te mappings.

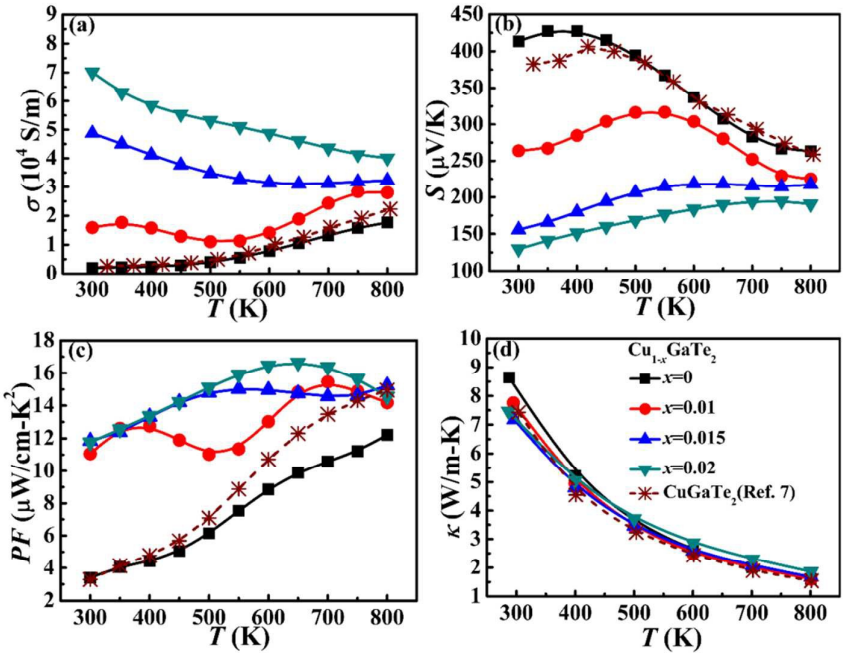

Fig. 3 Temperature dependence of (a)electrical conductivity (σ), (b)Seebeck coefficient (S), (c)power factors (PFs), and (d)thermal conductivity κ in $Cu_{1-x}GaTe_2$ (x = 0, 0.01, 0.015, 0.2) compounds, the dashed line is the data in Ref. 7.

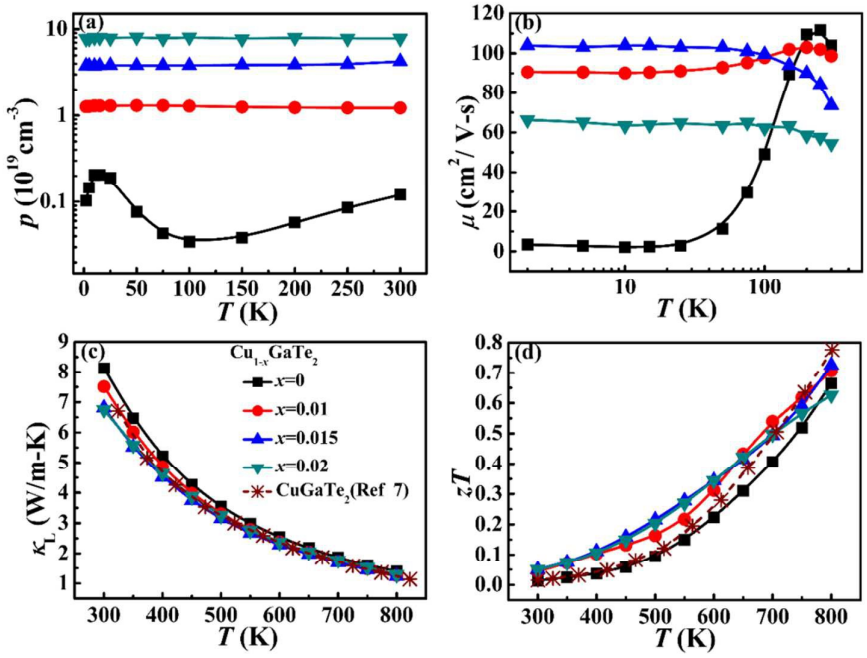

Fig. 4 Temperature dependence of (a)hole concentration, (b) Hall mobility μ_H, (c) lattice thermal conductivity κ_L, (d) zTs for $Cu_{1-x}GaTe_2$ (x = 0, 0.01, 0.015, and 0.2) compounds. The dashed line is the data in Ref. 7.

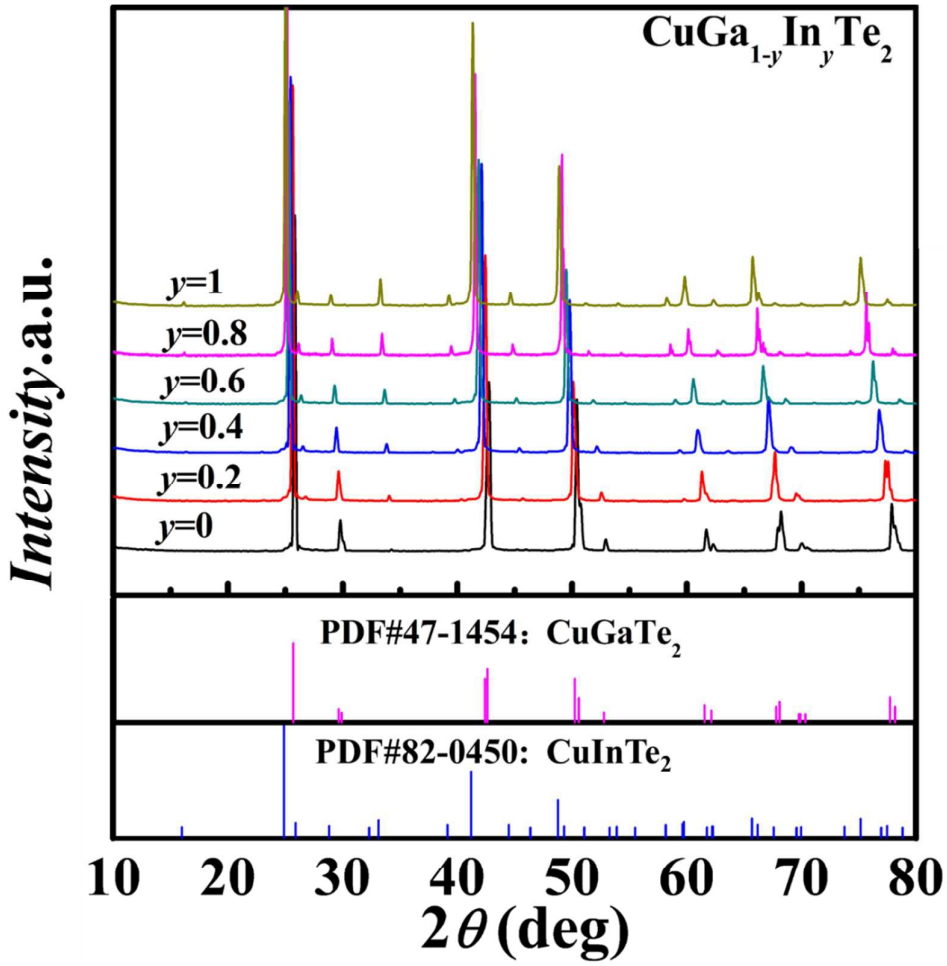

Fig. 5 Powder XRD patterns for $CuGa_{1-y}In_yTe_2$ (y = 0, 0.2, 0.4, 0.6, 0.8, and 1) samples.

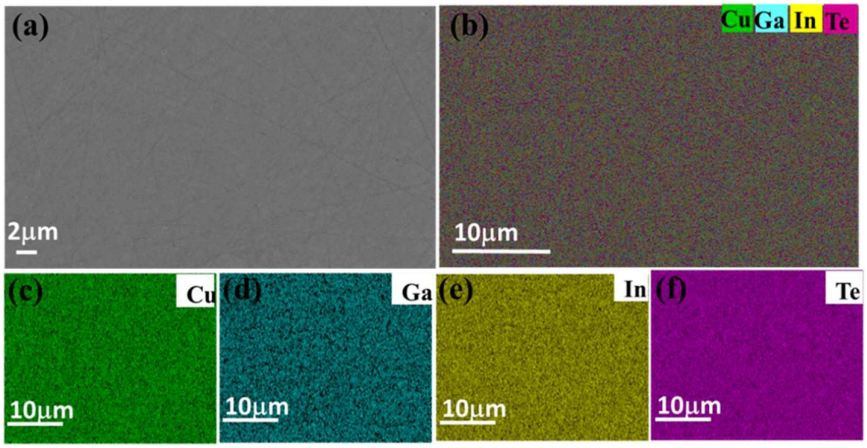

Fig. 6 Scanning electron microscopy (SEM) images of $CuGa_{0.6}In_{0.4}Te_2$ compound. (a) Backscattered electron imaging map, (b) all element, (c) Cu, (d) Ga, (e) In, and (f) Te mappings.

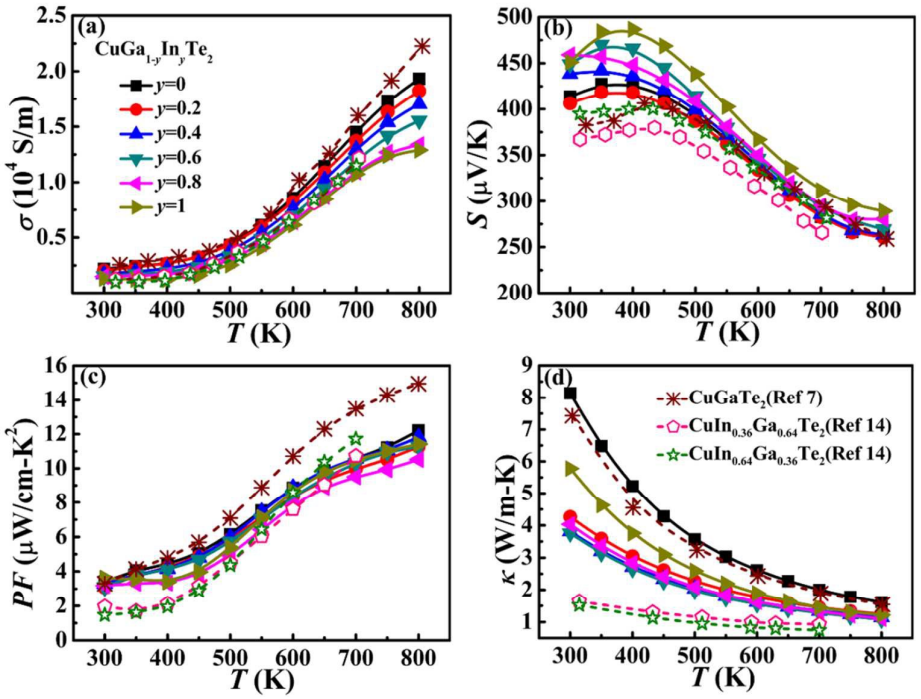

Fig. 7 Temperature dependence of (a) electrical conductivity (σ), (b) Seebeck coefficient (S), (c) power factors (PFs), and (d) thermal conductivity (κ) for $CuGa_{1-y}In_yTe_2$ (y = 0, 0.2, 0.4, 0.6, 0.8, and 1) compounds. The dashed lines are the data in Refs. 7 ,14.

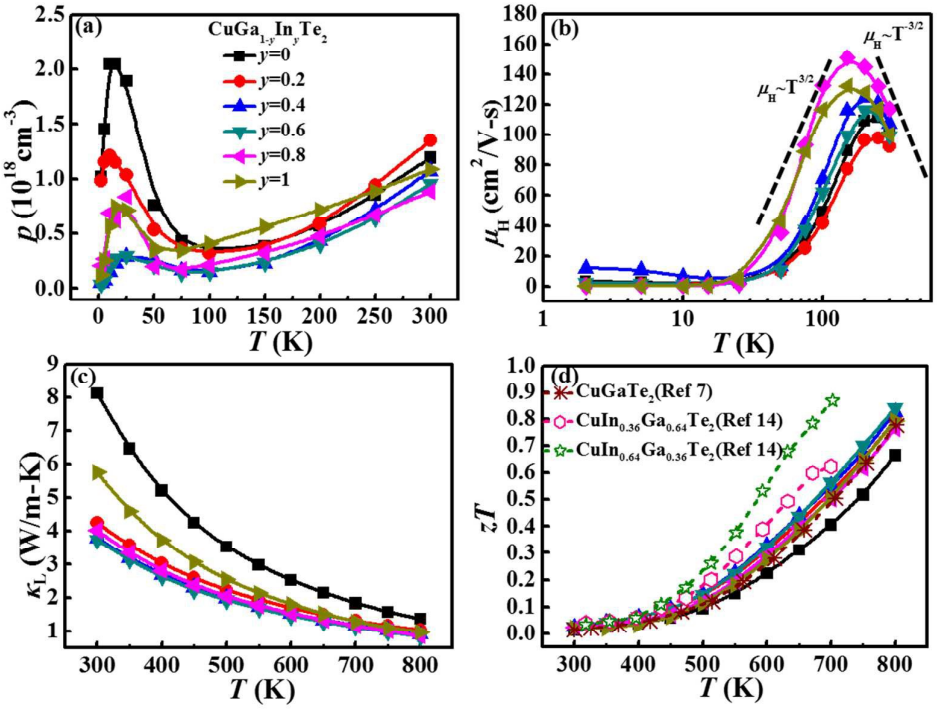

Fig. 8 Temperature dependence of (a) carrier concentration p, (b) Hall mobility μ_H, (c) lattice thermal conductivity κ_L, and (d) zTs for $CuGa_{1-y}In_yTe_2$ (y = 0, 0.2, 0.4, 0.6, 0.8, and 1) compounds.

The dashed lines are the data in Refs. 7 ,14.

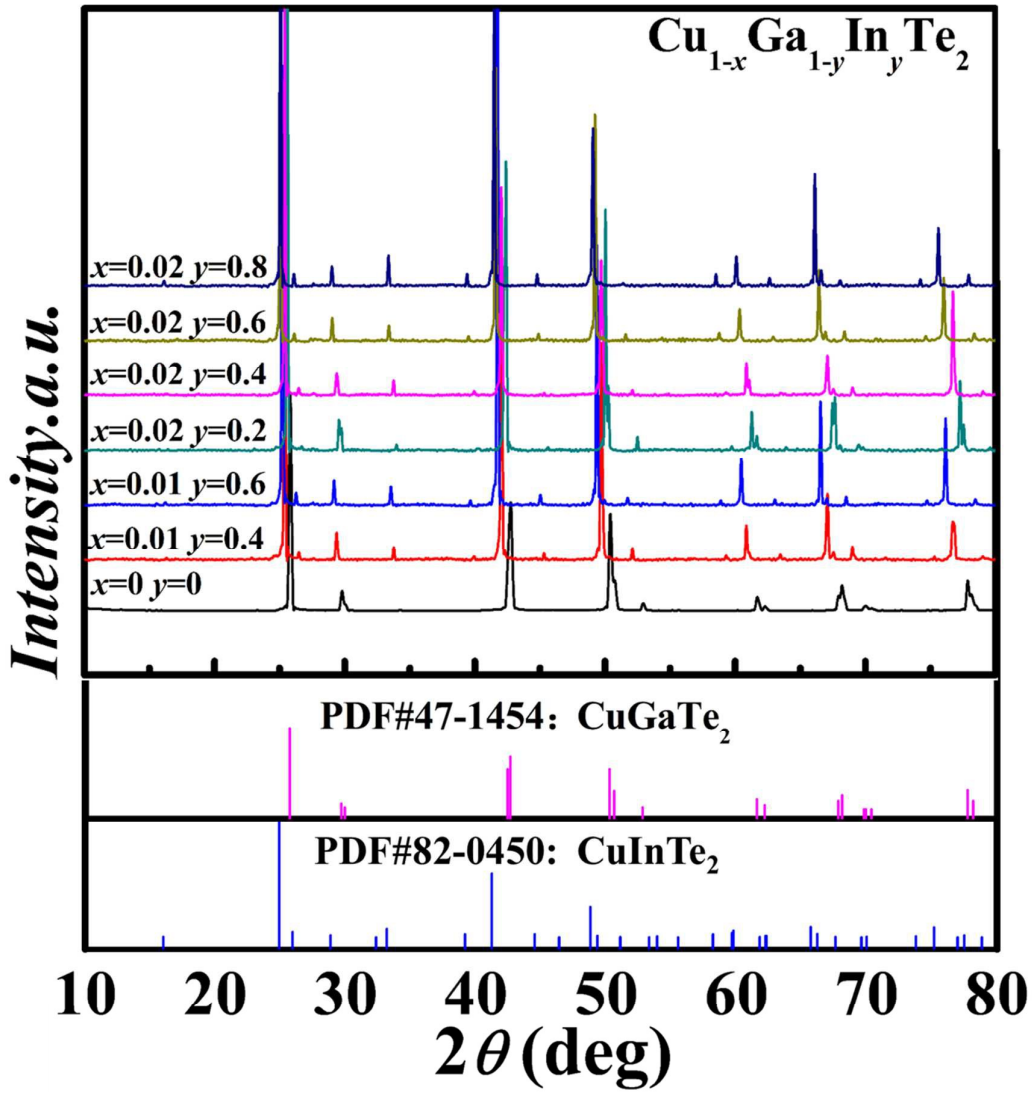

Fig. 9 Powder XRD patterns for $Cu_{1-x}(Ga_{1-y}In_y)Te_2$ (x = 0.01, 0.02, y = 0.2, 0.4, 0.6, 0.8) samples.

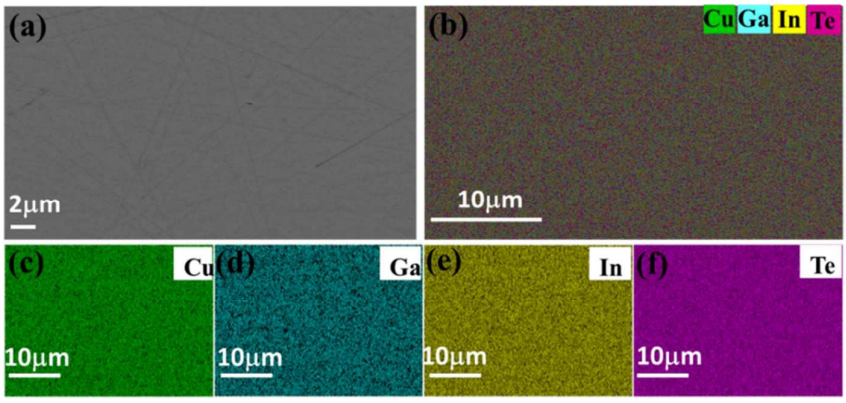

Fig. 10 Scanning electron microscopy (SEM) images of $Cu_{0.98}Ga_{0.6}In_{0.4}Te_2$ compound. (a) Backscattered electron imaging map, (b) all element, (c) Cu, (d) Ga, (e) In, and (f) Te mappings.

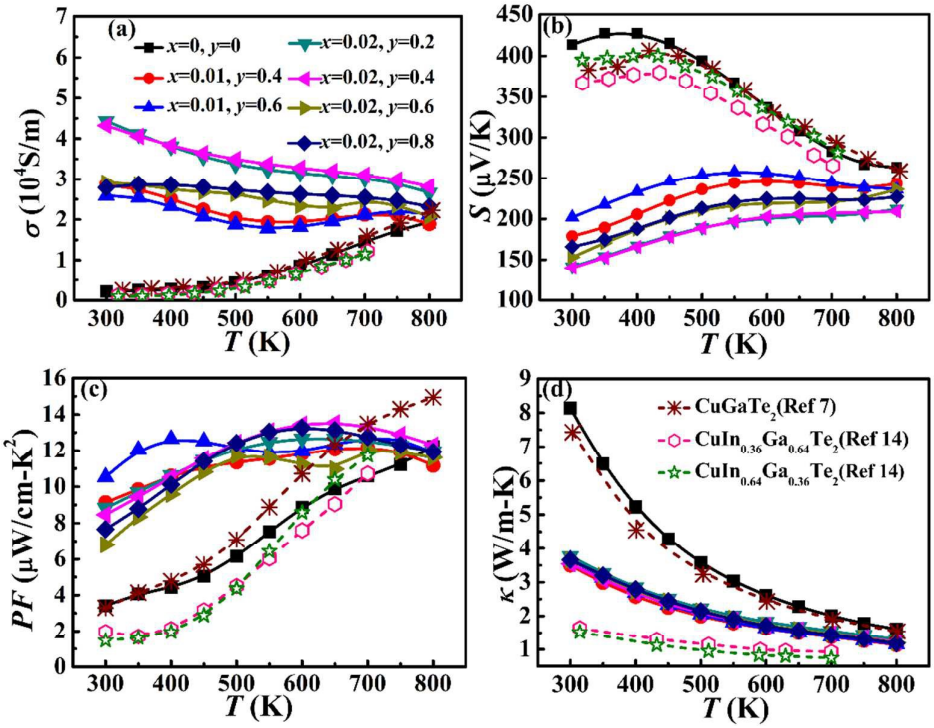

Fig. 11 Temperature dependence of (a) electrical conductivity (σ), (b) Seebeck coefficient (S), (c) power factors (PFs) , and (d) thermal conductivity (κ) for $Cu_{1-x}Ga_{1-y}In_yTe_2$ (x = 0.01, 0.02; y = 0.2, 0.4, 0.6, 0.8) samples. The dashed lines are the data in Refs. 7 and 14.

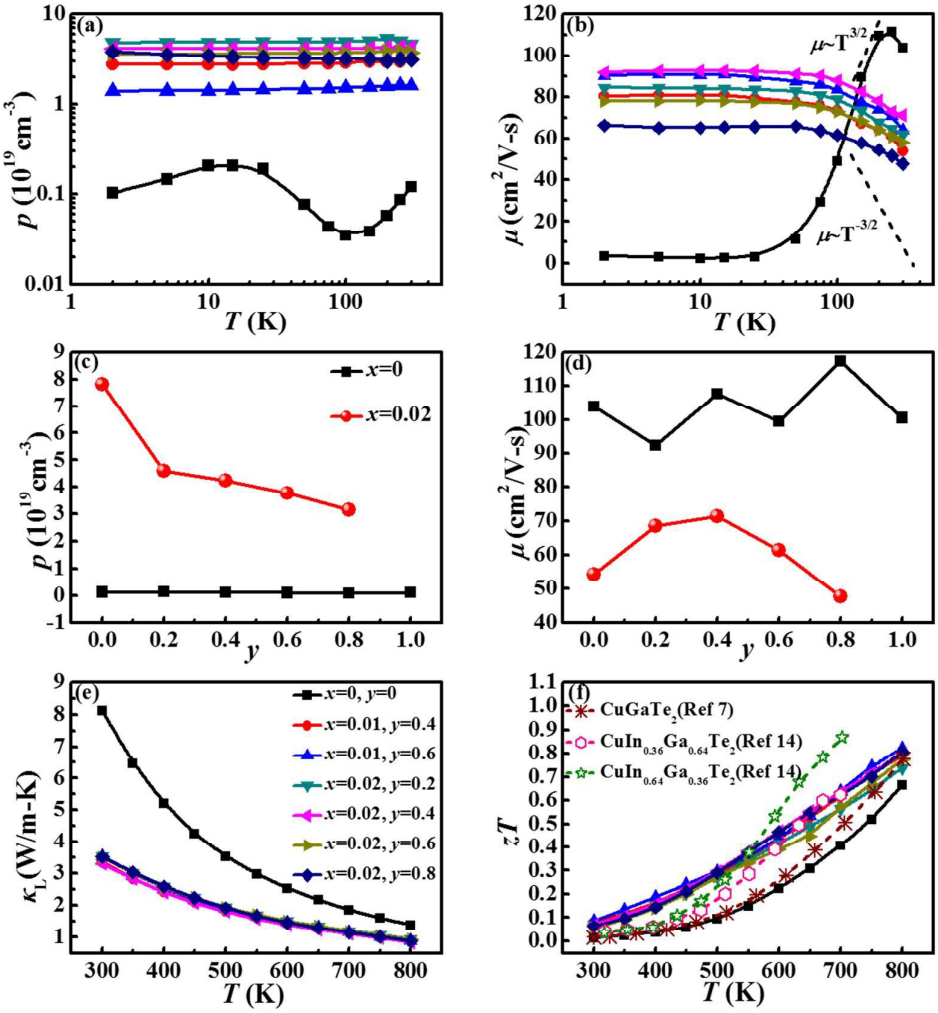

Fig. 12 Temperature dependence of (a) carrier concentration p and (b) Hall mobility μ_H, (c) hole concentration and (d) Hall mobility as a function of y (percentage content of Indium content) with varying x (percentage content of Cu-deficiency), and temperature dependence of (e) thermal conductivity κ and (f) zTs for $Cu_{1-x}(Ga_{1-y}In_y)Te_2$ (x = 0.01, 0.02, y = 0.2, 0.4, 0.6, and 0.8) compounds. The dashed lines are the data in Refs. 7 ,14.

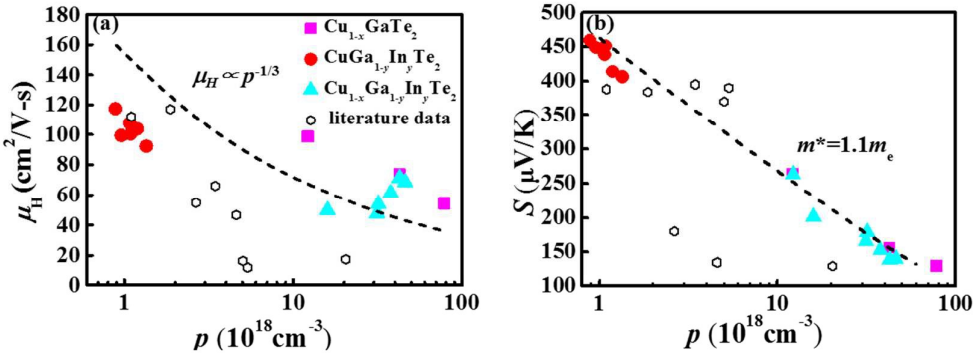

Fig. 13 (a) Room temperature Hall mobility and (b) Seebeck coefficient as a function of the hole concentration p for all the materials. The data from Refs. 5, 6 and 7 are also presented. The line in **Figure 13a** shows the curve of $\mu_H \propto p^{-1/3}$. The line in Fig. 13b is the calculated curve by single parabolic band model with $m^*=1.1m_e$.

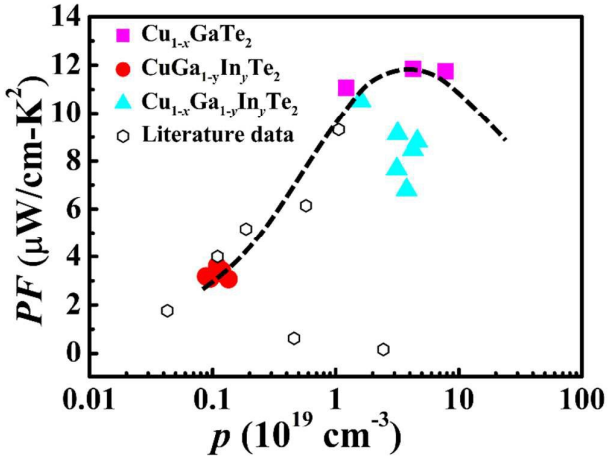

Fig. 14 Power factor at 300 K as a function of carrier concentration. The dashed line is a guide to the eyes.

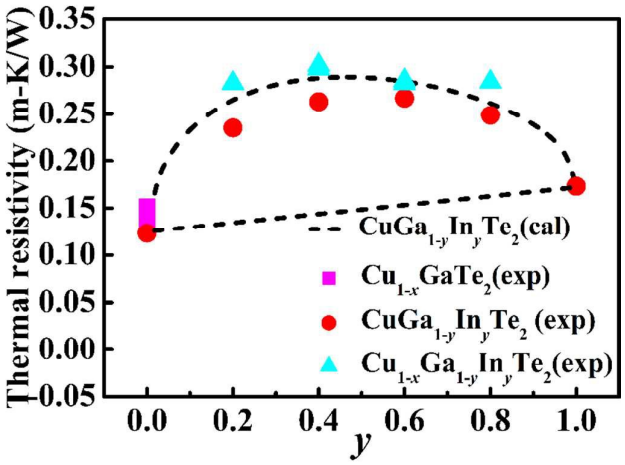

Fig. 15 Room temperature thermal resistivity (W) of $Cu_{1-x}Ga_{1-y}In_yTe_2$ (x = 0, 0.01 and 0.02; y = 0, 0.2, 0.4, 0.6, and 0.8) compounds as a function of Indium content y. The straight line represents the variation from the rule of mixtures. The curved line represented the additional thermal resistivity due to solid solution formation according to the theory of Callaway and Von Baeyer.

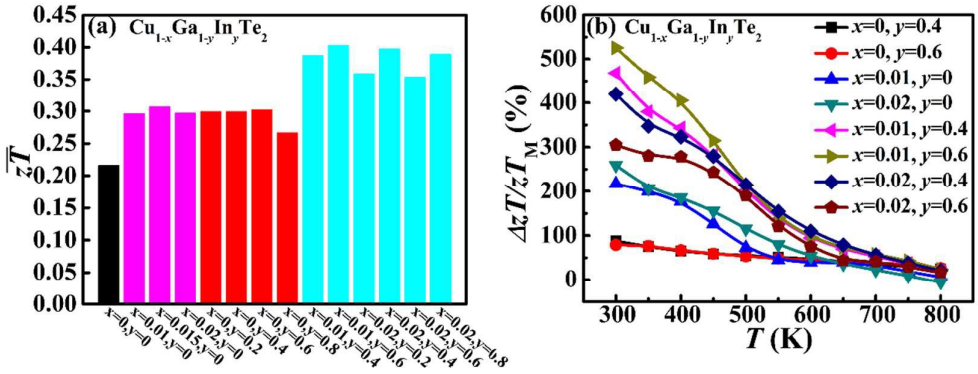

Fig. 16 (a) Average *zT*s for $Cu_{1-x}Ga_{1-y}In_yTe_2$ (x = 0, 0.01, and 0.02; y = 0, 0.2, 0.4, 0.6, and 0.8) samples from 300 K to 800 K, (b) Temperature dependence of the *zT* enhancement $\Delta(zT)/zT$ of $Cu_{1-x}Ga_{1-y}In_yTe_2$ (x = 0, 0.01, and 0.02; y = 0.4 and 0.6).

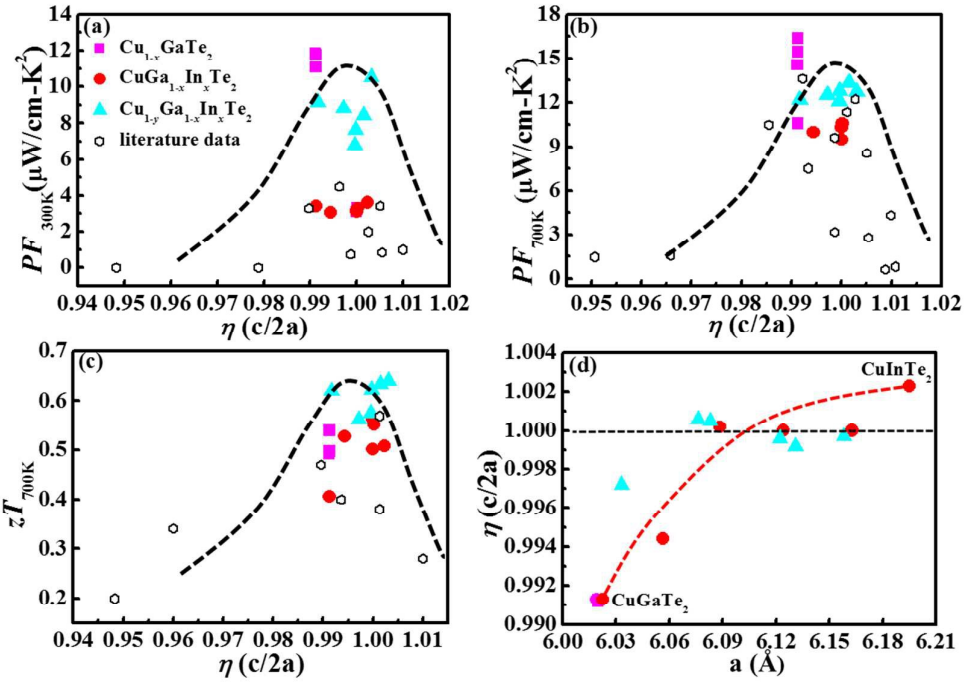

Fig. 17 (a) Power factors at 300 K, (b) Power factors at 700 K, (c) *zT*s at 700 K as a function of distortion parameter η, and (d) the distortion parameter η as a function of lattice constant a. The black dashed line in Fig. 17d represents $\eta = 1$. The red line in Fig. 17d is the calculated curve taken from Ref. 8. The other lines are guides to the eyes. The literature *PF*s and *zT*s are from Refs. 1, 5-7, 36-39.

TABLE 1. Lattice parameters and TE transport properties at 300 K for $Cu_{1-x}GaTe_2$, $CuGa_{1-y}In_yTe_2$, and $Cu_{1-x}(Ga_{1-y}In_y)Te_2$.

	a (Å)	c (Å)	η (c/2a)	σ (10^4S /m)	S (μV/K)	p (10^{19} cm^{-3})	μ_H (cm^2 /V-s)	m^* (m_e)
$CuGaTe_2$	6.0225(2)	11.9394(4)	0.9912	0.20	413	0.12	103.9	0.84
$CuInTe_2$	6.1949(3)	12.4190(1)	1.0023	0.13	451	0.11	100.4	1.06
$Cu_{0.99}GaTe_2$	6.0201(2)	11.9341(7)	0.9912	1.59	263	1.22	98.7	1.27
$Cu_{0.985}GaTe_2$	6.0198(2)	11.9343(3)	0.9913	4.88	156	4.26	73.7	1.10
$Cu_{0.98}GaTe_2$	6.0192(3)	11.9322(7)	0.9912	7.01	130	7.81	54.4	1.21
$CuIn_{0.2}Ga_{0.8}Te_2$	6.0564(1)	12.0451(4)	0.9944	0.20	406	0.13	92.3	0.86
$CuIn_{0.4}Ga_{0.6}Te_2$	6.0884(3)	12.1791(1)	1.0002	0.17	438	0.11	107.7	0.95
$CuIn_{0.6}Ga_{0.4}Te_2$	6.1241(1)	12.2473(2)	1.0000	0.15	449	0.10	99.4	0.96
$CuIn_{0.8}Ga_{0.2}Te_2$	6.1628(3)	12.3261(1)	1.0000	0.15	459	0.09	117.3	0.98
$Cu_{0.98}In_{0.2}Ga_{0.8}Te_2$	6.0332(8)	12.0323(2)	0.9972	4.10	141	4.60	68.5	1.01
$Cu_{0.98}In_{0.4}Ga_{0.6}Te_2$	6.0761(9)	12.1595(2)	1.0006	4.06	140	4.25	71.3	0.95
$Cu_{0.98}In_{0.6}Ga_{0.4}Te_2$	6.1221(3)	12.2396(2)	0.9996	2.86	153	3.77	61.3	0.99
$Cu_{0.98}In_{0.8}Ga_{0.2}Te_2$	6.1582(5)	12.3149(7)	0.9997	2.87	166	3.13	47.8	0.99
$Cu_{0.99}In_{0.4}Ga_{0.6}Te_2$	6.0803(9)	12.1667(3)	1.0005	2.75	179	3.19	53.9	1.12
$Cu_{0.99}In_{0.6}Ga_{0.4}Te_2$	6.1310(1)	12.2521(6)	0.9992	2.54	202	1.59	49.9	0.86

The table of contents entry:

Applying Cu-deficiency and In-alloying at Ga site simultaneously in the diamond-like pseudocubic $CuGaTe_2$ compounds can effectively adjust distortion parameters to be around unity, resulting in cubic-like degenerate band-edge electronic state thus greatly enhanced electrical performance. Combining with the reduced thermal conductivity, considerable TE performance has been achieved in pseudocubic $CuGaTe_2$-based compounds.

Keyword: thermoelectric, diamond-like, pseudocubic, distortion parameters

Authors:

Yuting Qin, Pengfei Qiu, Ruiheng Liu, Yulong Li, Feng Hao, Tiansong Zhang, Dudi Ren, Xun Shi,* and Lidong Chen*

Title: Optimized thermoelectric properties in pseudocubic diamond-like compounds

ToC figure: